ADVANCED MATERIALS INTERFACES
www.advmatinterfaces.de

Spin-Charge Conversion in Fe/Au/Sb_2Te_3 Heterostructures as Probed By Spin Pumping Ferromagnetic Resonance

*Emanuele Longo, Lorenzo Locatelli, Matteo Belli, Mario Alia, Arun Kumar, Massimo Longo, Marco Fanciulli, and Roberto Mantovan**

Large-area antimony telluride (Sb_2Te_3) thin films are grown by a metal organic chemical vapor deposition technique on 4" Si(111) substrates, and their topological character probed by magnetoconductance measurements. When interfaced with Fe thin films, broadband ferromagnetic resonance spectroscopy (BFMR) shows a clear increase of the damping parameter in Fe/Sb_2Te_3 when compared to a reference Fe layer, which may suggest the occurrence of spin pumping (SP) into Sb_2Te_3. Simultaneously, X-ray reflectivity and conversion electron Mossbauer spectroscopy evidence the development of a chemically and magnetically pure Fe/Sb_2Te_3 interface. However, by conducting SP-FMR, it is shown that no spin-to-charge conversion (S2C) occurs in Fe/Sb_2Te_3, while a clear SP signal develops by introducing a 5 nm Au interlayer between Fe and Sb_2Te_3, with a measured inverse Edelstein effect conversion efficiency of $\lambda_{IEE} = 0.27$ nm. The results shed some light on the correlation among the chemical-structural-magnetic properties of the Fe/Sb_2Te_3 interface, the broadening of the magnetic damping parameter as detected by BFMR, and the occurrence of S2C, as probed by SP-FMR.

1. Introduction

Topological insulators (TI) are gaining attention from a technological point of view due to their foreseen highly efficient capability to control adjacent magnetic media and to act as ideal spin sinks through spin-to-charge conversion (S2C) phenomena.[1] Clarifying the role played in S2C by the specific chemical bonds and/or the presence of magnetically dead-layers and/or intentionally-grown interlayers at the interface between TI and ferromagnetic (FM) layers is highly demanding.[2–4] Additionally, in view of realizing a step toward technology transfer, developing fabrication methods suitable to guarantee the large-scale production of TI is necessary.

The Metal Organic Chemical Vapor Deposition (MOCVD) process has recently been successful in growing epitaxial-quality TI, such as antimony telluride (Sb_2Te_3) and bismuth telluride (Bi_2Te_3) on 4" Si(111) substrates, being characterized by the typical Van der Waals stacking order.[5,6] In particular, Sb_2Te_3 layers are characterized by the expected rhombohedral crystalline structure belonging to the *R*-3*m* space group.[7–9]

In the present manuscript, we show that epitaxial Sb_2Te_3 layers on Si(111) manifest improved magnetoconductance (MC) performances when compared to the "granular" Sb_2Te_3 obtained on SiO_2,[10,11] and we probe S2C in heterostructures formed by Fe/Sb_2Te_3 and Fe/Au/Sb_2Te_3 stacks by making use of broadband ferromagnetic resonance spectroscopy (BFMR) and spin pumping FMR (SP-FMR).

Following the deposition of Fe layers in direct contact with Sb_2Te_3, BFMR evidences a clear increase of the damping parameter from $23 \cdot 10^{-3}$ in the reference Au/Fe/Si(111) to $41 \cdot 10^{-3}$ in Au/Fe/Sb_2Te_3, where epitaxial Sb_2Te_3 is obtained following proper thermal processing.[5] Simultaneously, X-ray reflectivity (XRR) and conversion electron Mössbauer spectroscopy (CEMS) evidence the development of a chemically and magnetically pure interface. However, by conducting SP-FMR, we show that no S2C occurs when Fe is in direct contact with epitaxial Sb_2Te_3, while a clear SP signal emerges when a 5 nm Au interlayer is introduced to fabricate an Au(5 nm)/Fe(5 nm)/Au(5 nm)/Sb_2Te_3/Si(111) heterostructure. By interpreting the S2C conversion with the inverse Edelstein effect (IEE), a conversion efficiency of $\lambda_{IEE} \approx 0.27$ nm is obtained, in good agreement with that previously observed in Co/Sb_2Te_3 systems.[4] Our results point to the conclusion that the observed S2C, as detected by SP-FMR in Fe/Au/Sb_2Te_3, originates from the topologically protected surface states (TSS) of Sb_2Te_3, which are likely detrimentally affected when depositing Fe in direct contact with Sb_2Te_3.

2. Results and Discussion

Table 1 summarizes the structure of the samples being the subject of the present work. In the AS DEP, PRE ANN, and POST

E. Longo, L. Locatelli, M. Belli, M. Alia, A. Kumar, M. Longo,[+] R. Mantovan
CNR-IMM
Unit of Agrate Brianza
Via Olivetti 2, Agrate Brianza (MB) I-20864, Italy
E-mail: roberto.mantovan@mdm.imm.cnr.it
M. Fanciulli
Università degli studi di Milano-Bicocca
Dipartimento di Scienze dei Materiali
Via R. Cozzi 55, Milano 20126, Italy

The ORCID identification number(s) for the author(s) of this article can be found under https://doi.org/10.1002/admi.202101244.

[+]Present address: CNR-IMM, Unit of Rome, Via Fosso del Cavaliere, 100, Rome I-00133, Italy

DOI: 10.1002/admi.202101244

Table 1. List of the heterostructures analyzed in the manuscript.

Sample	Stack with layers' nominal thickness
REF	Si(111)/^{57}Fe(5 nm)/Au(5 nm)
AS DEP	Si(111)/Sb_2Te_3(30 nm, As-dep)/^{57}Fe(5 nm)/Au(5 nm)
PRE ANN	Si(111)/Sb_2Te_3(30 nm, Pre-ann)/^{57}Fe(5 nm)/Au(5 nm)
POST ANN	Si(111)/Sb_2Te_3(30 nm, Post-ann)/^{57}Fe(5 nm)/Au(5 nm)
REF-IL	Si(111)/Au(5 nm)/^{57}Fe(5 nm)/Au(5 nm)
POST ANN-IL	Si(111)/Sb_2Te_3(30 nm, Post-ann)/Au(5 nm)/^{57}Fe(5 nm)/Au(5 nm)

ANN heterostructures, the only difference is in the Sb_2Te_3 preparation (see Experimental Section).[5]

The evaporated Fe and Au layers are polycrystalline, see Figure S1 in the Supporting Information. The post-growth annealing of Sb_2Te_3 triggers a reorganization of the film grains, favoring the formation of highly-oriented layers, being characterized by a surface mean roughness (as detected by atomic force microscopy) around 1 nm.[5] A scanning electron microscopy image of the post-annealed Sb_2Te_3 is shown in Figure S2 in the Supporting Information. Moreover, the total reflection X-ray fluorescence spectrometry analysis showed mainly the presence of Sb and Te, with no additional elemental signals detected, thus demonstrating the absence of undesired contaminants in the Sb_2Te_3 layers, see Supporting Information (Figure S3, Supporting Information)."

2.1. Magnetotransport in Extended Sb_2Te_3 on Si(111)

Figure 1a shows the MC (expressed by $\Delta\sigma$ in units of e^2/h) recorded at 10 K for the Sb_2Te_3 layers in AS DEP, PRE ANN, and POST ANN samples prior to the Fe/Au depositions. A clear non-parabolic perturbation is observed for the POST ANN sample. As a matter of fact, the MC data in all samples display a deviation from pure Lorentzian parabolic contribution, which is attributed to weak antilocalization (WAL) emerging at low temperature in the presence of highly conductive 2D states, due to intense spin-orbit coupling (SOC). Typically, the presence of WAL in TI is associated with the existence of TSS that contribute to the global conduction mechanisms.[12–15] In the framework of the Hikami-Larkin-Nagaoka (HLN) model,[11] the parameters α_{HLN} (being connected to the number of 2D conducting channels), and the spin coherence length (l_φ), can be extracted following the fit of the MC curves, and the results are shown in Figure 1b.

Regardless of the thermal processing to which they are subjected,[5] all the Sb_2Te_3 layers exhibit WAL, and the extracted α_{HLN} ranges from 0.1 to 0.3. These values are lower than the 0.5 expected in the case of a single conductance channel (likely the surface), indicating that there is still a contribution from the bulk states. Indeed, all the layers show a consistent decrease of their sheet resistance (R_S) upon cooling (not shown) that, together with the high holes density (≈10^{20} cm^{-3}), suggests a relevant participation of bulk states in the global conduction mechanism. The R_S of Sb_2Te_3 layers lowers with thermal processing (insets in Figure 1b), due to their improved crystalline quality.[5] This is reflected in the marked increase of l_φ from 31 nm for as-deposited Sb_2Te_3 up to 60 nm in the post-annealed Sb_2Te_3 layer.

It is interesting to note how, even in the as-deposited Sb_2Te_3, there is a relatively high α_{HLN}, being much higher (at same T) than that observed in as-deposited Sb_2Te_3 grown on SiO_2, while the l_φ is lower.[11] We attribute the higher α_{HLN} on top of Si(111) as due to a better intra-granular structural quality when compared to Sb_2Te_3 films on top of SiO_2, while the lower l_φ may be connected to a higher density of grain boundaries, limiting the transverse spin-coherence length.

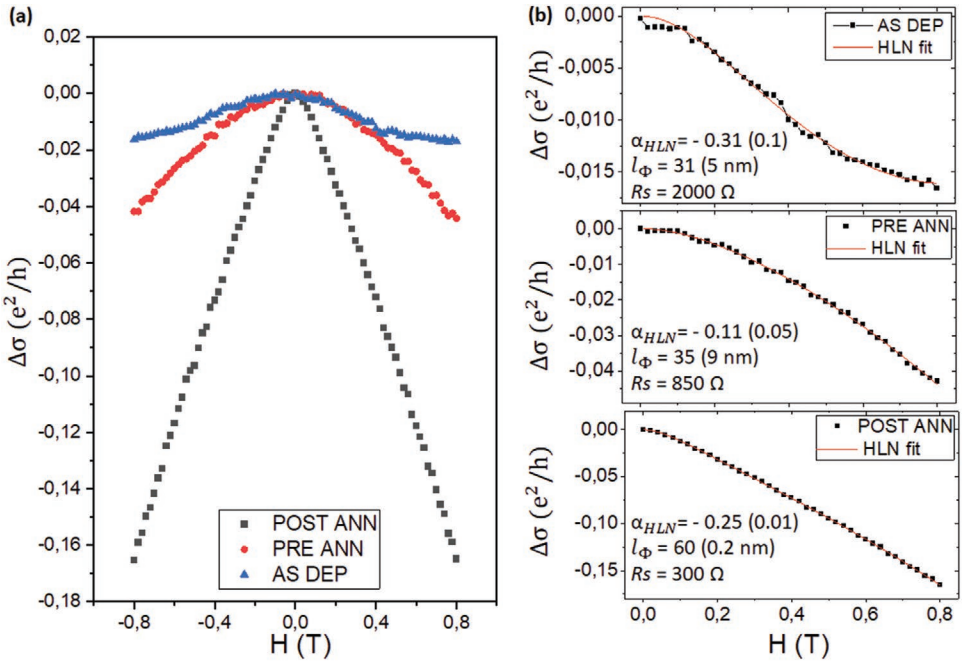

Figure 1. Comparison of the a) MC in Sb_2Te_3 (prior to the Fe/Au deposition) in the AS DEP, PRE ANN and POST ANN samples, recorded at 10 K. The data are expressed in (e^2/h) unit and referred to their zero-field. b) HLN fit of the MC data, with the values of the α_{HLN} and l_φ parameters.

2.2. Chemical, Structural, and Magnetic Characterization of the Fe/Sb_2Te_3 Interface

In **Figure 2**, the chemical-structural analysis carried out by XRR on the whole set of samples listed in Table 1 is shown. Here, the collected data (black solid line) are fitted with a multilayer model and the best fit is represented by a red solid line. For the AS DEP sample, it is not possible to conduct a useful fit. This is caused by its high surface roughness of 3.9 nm.[5] This value is comparable to the nominal 5 nm-thickness of the ^{57}Fe layer evaporated on top (Table 1), thus originating a non-uniform distribution of the Fe thickness, likely promoting a partial coverage of the Sb_2Te_3 surface. Indeed, the Croce-Nevot XRR model can be successfully employed for samples with a stacking order not too far from a multilayered system, where the levels of the interdiffusion or structural inhomogeneities are restrained.[16]

Differently, clear XRR oscillations emerge in the PRE ANN and POST ANN samples (Figure 2a), showing how the improved structure and morphology of the developed epitaxial Sb_2Te_3 directly reflects in the development of a well-controlled Au/Fe/Sb_2Te_3 heterostructure. From XRR, a high chemical-structural quality is observed also for the REF-IL and POST ANN-IL samples, demonstrating the successful integration of the Au interlayer in separating the Fe layer from the Sb_2Te_3 at the bottom of the stack (Figure 2b).

The extracted XRR parameters for all the samples are summarized in **Table 2**. It is clear how very few differences are observed between the Au/Fe bilayers on the REF sample and the annealed Sb_2Te_3 underlayer. In the PRE ANN and POST ANN samples, we detect denser Au layers and thinner Fe layers, when compared to the REF sample. This is attributed to the different surface roughness of Si(111) and Sb_2Te_3, being respectively ≈10% and ≈50% of the total Fe thickness (Table 2). We conclude that an overall good chemical-structural quality exists for the REF, PRE ANN and POST ANN samples. Similarly to the interlayer-free samples, we detected a higher roughness roughness for the Au/Fe/Au layers deposited on top of Sb_2Te_3 with respect to Si(111) in the POST ANN-IL and REF-IL samples, respectively. On the other hand, the almost identical electronic densities for the layers in those

Table 2. XRR parameters extracted from the fit shown in Figure 2. The error bars are ± 0.1 nm for the thickness (and roughness), and ± 0.05 e^- Å^{-3} for the electronic densities.

	Layer	Nominal Thickness [nm]	Measured Thickness [nm]	$\rho(e^-$ Å$^{-3})$	Roughness [nm]
REF	Au	5	4,7	5,0	0,48
	Fe	5	5,6	2,2	0,55
	Si(111)	/	/	0,72	0,4
PRE ANN	Au	5	4,0	4.1	1,6
	Fe	5	3,7	2,2	1.7
	Sb_2Te_3	30	30	1.2	1.5
POST ANN	Au	5	4,2	4.0	1,5
	Fe	5	3,1	2,2	1,7
	Sb_2Te_3	30	31	1,3	1,4
REF-IL	Au	5	4,3	4,5	0,6
	Fe	5	5,8	2,3	1,0
	Au	5	4,8	4,5	0,4
	Si(111)	/	/	0,72	0,4
POST ANN-IL	Au	5	4,4	4,2	1,2
	Fe	5	4,5	2,4	1,2
	Au	5	5,4	4,2	1,3
	Sb_2Te_3	30	28	1,5	0,9

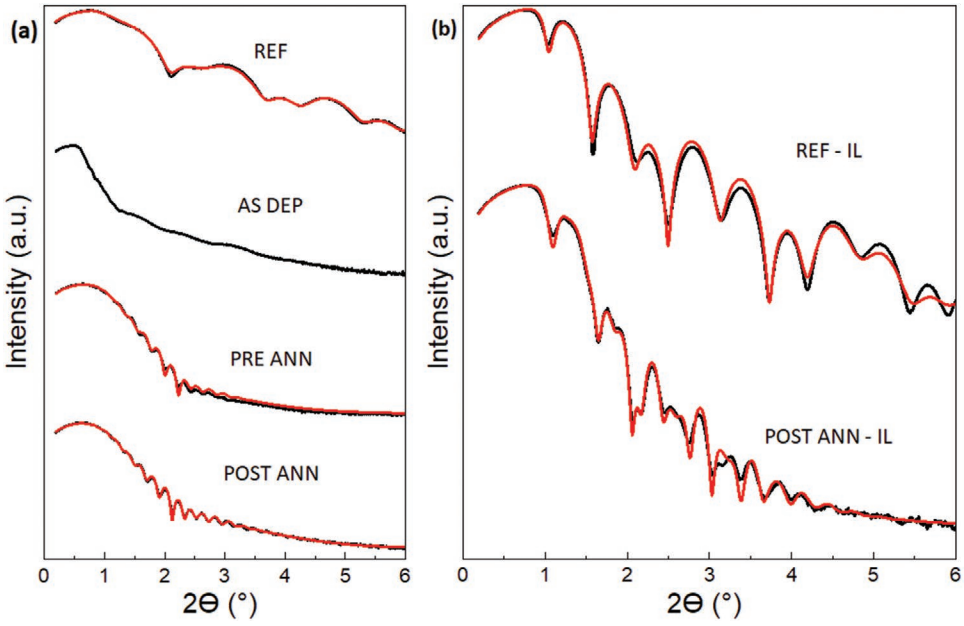

Figure 2. XRR collected data for the samples a) without and b) with Au interlayer, as listed in Table 1 (black solid line). The best fit of the curves is represented by the red solid lines and the extracted parameters are summarized in Table 2. As substantiated in the text, for the AS DEP sample a reliable XRR model could not be found due to the relatively high roughness of un-treated Sb_2Te_3.

samples, demonstrates the good reproducibility of the Au/Fe/Au deposition process on top of Sb_2Te_3 and Si(111).

Conversion-electron Mössbauer spectroscopy (CEMS) is conducted on all the samples indicated in Table 1, and the results depicted in **Figure 3**. In the Fe/Sb_2Te_3 structures that we previously discussed in refs. [7,10], pulsed laser deposition was employed to grow a ≈1 nm ^{57}Fe layer in direct contact with Sb_2Te_3, then capped by a few nm of non-CEMS sensitive ^{54}Fe. The main difference with the set of samples here under study (Table 1) is that 100% of isotopically enriched ^{57}Fe layers are used. Consequently, CEMS probes both the top Au/Fe and bottom Fe/Sb_2Te_3 interfaces in AS DEP, PRE ANN and POST ANN, the two Au/Fe and Fe/Au interfaces in REF-IL and POST ANN-IL, and of course the whole Fe layer in all the samples. It is demanding to separate the contribution in the spectra from the top Au/Fe, in order to monitor the changes occurring at the bottom Fe/Sb_2Te_3 interface depending on the Sb_2Te_3 preparation (Table 1).

We adopt the following fitting strategy. First, the REF sample of Figure 3a is analyzed, with the aim of identifying the hyperfine parameters for the components originating at the top Au/Fe interface. These are used, and fixed (except where indicated), in the AS-DEP, PRE ANN, and POST ANN samples in Figure 3b–d, since the Au/Fe deposition is done at RT in all the samples following identical procedures and without any post-growth processing.

The CEMS-spectrum for the REF sample is dominated by a magnetically-split sextet (green SEXTET in Figure 3) that is attributed to α-Fe, with a B_{hf} slightly lower than the bulk case (32.9 T) as often observed in thin films.[17] Additionally, a small magnetic component DIST is detected (yellow in Figure 3), together with two paramagnetic doublets DOUB-1 and DOUB-2, respectively red and orange in Figure 3. All these components are still present in the PRE ANN and POST ANN samples, plus an additional paramagnetic doublet DOUB-3 (shown in Figure 3). In the REF-IL and POST ANN-IL samples, we detect α-Fe, DIST and only the DOUB-1 paramagnetic component. All the parameters extracted from the fit of all the CEMS-spectra depicted in Figure 3, are summarized in **Table 3**.

The DIST in REF is due to Fe atoms partially mixing with Au at the Au/Fe interface.[18] In the AS DEP, PRE ANN and AS DEP samples, DIST now also contains the contribution from the bottom Fe/Sb_2Te_3 interface.[7,10] However, due to the relatively low spectral intensity of the DIST component, we keep a unique distribution of sextets in the fit of the AS-DEP, PRE ANN and POST ANN CEMS signal, where the contribution from the bottom Fe/Sb_2Te_3 interface becomes dominant, as indicated by the lower isomer shift when compared to the DIST in REF (Table 1), which is now very similar to that observed at the Fe/Sb_2Te_3 interfaces.[7,10] The nature of the DIST component seems not to be very much affected by the Sb_2Te_3 preparation (Figure 3 and Table 3).

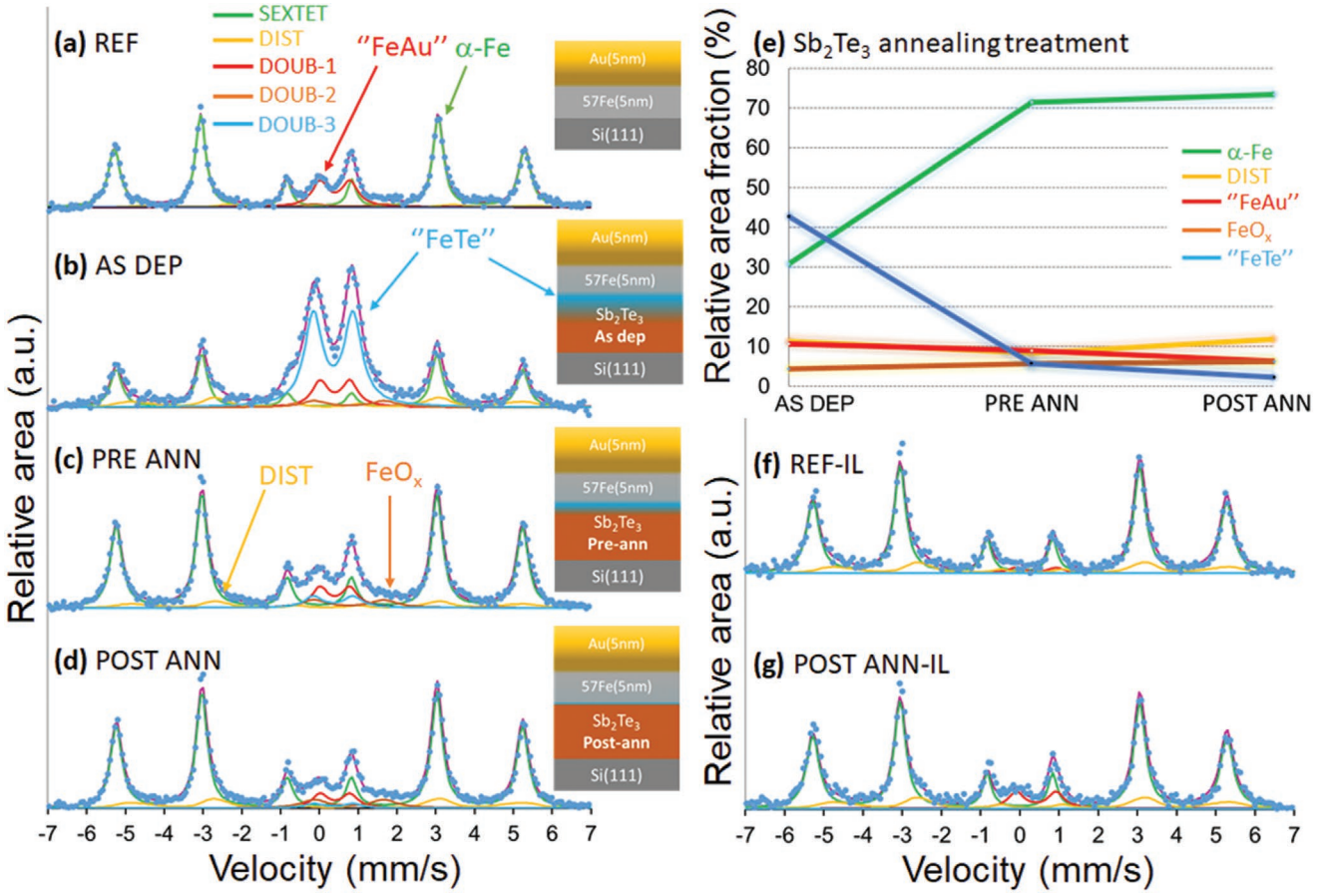

Figure 3. CEMS spectra of samples a) REF and b–d) AS DEP, PRE ANN, POST ANN; e) evolution of the relative fractions of the spectral components detected in the AS DEP, PRE ANN, and POST ANN samples. f,g) CEMS spectra of samples REF-IL and POST ANN-IL containing the Au interlayer.

Table 3. Hyperfine parameters for all the spectral components used to interpret the CEMS data shown in Figure 3, for the full set of samples of Table 1.

	Hyperfine parameters	α-Fe	DIST	DOUB-1	DOUB-2	DOUB-3
REF	$<B_{hf}>$ (T)	32.75(1)	30.7(1)	–	–	–
	δ (mm s^{-1})	0.0	0.55(3)	0.400(4)	0.76(4)	–
	ΔE_Q (mm s^{-1})	0.0	0	0.77(1)	1.8(1)	–
	$<\Gamma>$ (mm s^{-1})	0.32(1)	0.5	0.5	0.8(1)	–
	A_{25}	4	4	–	–	–
AS DEP	$<B_{hf}>$ (T)	32.43(2)	30.7(1)	–	–	–
	δ (mm s^{-1})	0.0	0.19(2)	0.40(1)	0.76(5)	0.356(2)
	ΔE_Q (mm s^{-1})	0.0	0	0.77(1)	1.80(9)	1.020(4)
	$<\Gamma>$ (mm s^{-1})	0.34(3)	0.5	0.5	0.81(6)	0.555(4)
	A_{25}	4	4	–	–	–
PRE ANN	$<B_{hf}>$ (T)	32.43(1)	30.7(1)	–	–	–
	δ (mm s^{-1})	0.0	0.19(1)	0.40(1)	0.76(4)	0.36(2)
	ΔE_Q (mm s^{-1})	0.0	0	0.77(2)	1.80(7)	1.02(3)
	$<\Gamma>$ (mm s^{-1})	0.34(3)	0.5	0.5	0.81(4)	0.55(2)
	A_{25}	4	4	–	–	–
POST ANN	$<B_{hf}>$ (T)	32.43(1)	30.7(1)	–	–	–
	δ (mm s^{-1})	0.0	0.19(1)	0.40(1)	0.76(2)	0.36(4)
	ΔE_Q (mm s^{-1})	0.0	0	0.77(2)	1.80(4)	1.0(1)
	$<\Gamma>$ (mm s^{-1})	0.34(3)	0.5	0.5	0.81(3)	0.55(6)
	A_{25}	4	4	–	–	–
REF-IL	$<B_{hf}>$ (T)	32.70(1)	30.7(1)	–	–	–
	δ (mm s^{-1})	0.0	0.29(2)	0.41(1)	–	–
	ΔE_Q (mm s^{-1})	0.0	0.0	1.02(2)	–	–
	$<\Gamma>$ (mm s^{-1})	0.35(1)	0.5	0.5	–	–
	A_{25}	4	4	–	–	–
POST ANN-IL	$<B_{hf}>$ (T)	32.70(1)	30.7(1)	–	–	–
	δ (mm s^{-1})	0.0	0.29(2)	0.41(1)	–	–
	ΔE_Q (mm s^{-1})	0.0	0.0	1.02(2)	–	–
	$<\Gamma>$ (mm s^{-1})	0.35(1)	0.5	0.5	–	–
	A_{25}	4	4	–	–	–

DOUB-1 in the REF sample could potentially originate from both the top Au/Fe or/and the bottom Fe/Si interface(s). It is well known that Fe and Si have a certain reactivity even at RT, and paramagnetic doublets arise in the CEMS spectra[19,20] Indeed, FeSi and FeAu components may have a similar quadrupole splitting around 0.7 mm s^{-1} as we detect.[18,20] Being the observed isomer shift of 0.4 mm s^{-1} (Table 3) very close to that expected at the Au/Fe interface,[18] we tend to attribute DOUB-1 mostly to the top Au/Fe interface, even if a partial contribution to the spectral intensity from FeSi cannot be ruled out. DOUB-1 is indicated with "FeAu" in Figure 3.

In the REF-IL and POST ANN-IL samples, the top Au/Fe/Au trilayer is deposited simultaneously on Si(111) and Sb_2Te_3, and as expected they show basically identical CEMS signals. In both samples, there is the dominating magnetically-split sextet of α-Fe (≈81% in REF-IL and ≈77% in POST ANN-IL). The rest of the spectral intensity originates from magnetic (DIST) and paramagnetic (DOUB-1) Fe-Au interactions. Fe atoms in the DIST component are taking up to 16% and 15% of the total intensity in REF-IL and POST ANN-IL, respectively. The paramagnetic doublet DOUB-1 accounts for ≈3% and ≈8% intensity in REF-IL and POST ANN-IL respectively, likely reflecting the lower surface roughness of Si(111) when compared to Sb_2Te_3, giving rise to smoother top Au/Fe/Au interfaces in REF-IL, in which Fe atoms better retain their magnetic ordering.

The AS DEP CEMS-spectrum (Figure 3b) has an overall shape much well-resembling those previously observed at the interface in the $^{54}Fe/^{57}Fe$(1 nm)/$Sb_2Te_3/SiO_2/Si$ heterostructures.[7,10] AS DEP displays a dominant central paramagnetic component, for which the hyperfine parameters do not match those of DOUB-1 in REF. As anticipated, through the fully ^{57}Fe-enriched Fe layer, CEMS now explores the whole 5 nm-thick Fe layer and the additional top Au/Fe interface (Table 1). Therefore, in the fit of AS DEP we first include the DOUB-1 attributed to the top Au/Fe interface, as identified in the REF sample (Table 1) and keep fixed its hyperfine parameters in the fit of all

the Sb_2Te_3-containing samples (Table 3). It is clear how in the AS DEP sample, adding an additional doublet named DOUB-3 is necessary to justify the large central spectral intensity. This paramagnetic contribution undoubtedly originates from the bottom Fe/Sb_2Te_3 interface.

To fit the CEMS of the PRE ANN and POST ANN samples, the hyperfine parameters of all the components previously identified in REF and AS DEP are kept constant, except the relative area intensities, the DIST's isomer shift and the α-Fe's B_{hf} (Table 3). In Fe/Sb_2Te_3(granular)/SiO_2/Si, the central paramagnetic doublet has been assigned to the formation of a FeTe-type of the compound at the Fe/Sb_2Te_3 interface,[7,10] and we attribute DOUB-3 to the formation of a "FeTe" coordination that affects 43% of the Fe atoms in the AS DEP sample. The isomer shift of the DOUB-3 component is in good accordance with those previously reported, with a larger quadrupole splitting,[7,10] thus indicating a highly disordered environment around Fe. This is most likely due to the very large surface roughness up to 3.9 nm of the as deposited Sb_2Te_3 on Si(111),[5] being basically of the order of the nominal Fe thickness. Indeed, the surface roughness of the as-deposited Sb_2Te_3 on SiO_2 was of the order of ≈2 nm,[11] on top of which, most likely, Fe layers grow with a slightly higher conformality, thus generating Fe components with lower quadrupole splitting than in the case of AS DEP. Also, in refs. [7,10] the Fe thickness was ≈10 nm, thus certainly providing a more uniform layer.

A marginal Fe oxidation is detected through DOUB-2 in AS DEP, PRE ANN, and POST ANN samples, see Figure 3e, which apparently do not evolve with the thermal history of Sb_2Te_3. No oxidation is detected in samples REF-IL and POST ANN-IL. The insets in Figure 3a–d show a pictorial view of how the different components identified by CEMS in the samples without Au interlayer may be spatially distributed in the Au/Fe/Sb_2Te_3 heterostructures.

Figure 3e shows the evolution of the relative spectral intensity for all the components identified from the fit of the AS DEP, PRE ANN, and POST ANN samples. The main effect of the Sb_2Te_3 thermal processing is to induce a collapse of the "FeTe" contribution, promoting a good quality Fe/Sb_2Te_3 interface, with the CEMS data of the POST ANN (Figure 3d) basically resembling that of the REF sample (Figure 3a). We underline a remarkable difference between the evolution of the quality of the Fe/Sb_2Te_3 interface (both structurally and magnetically) following the Sb_2Te_3 growth on SiO_2,[10] with that now observed on Si(111). In the former case, the annealing of the Sb_2Te_3 prior to Fe deposition has been shown to have no influence on the relative abundance of the interface FeTe-type of bonding, with a constant fraction of 15–20% detected.[10] This is strikingly different from the case of Sb_2Te_3 on Si(111) here presented, where already the pre-annealing of the Si(111) before the Sb_2Te_3 deposition has an immediate effect in reducing the central paramagnetic component at the Fe/Sb_2Te_3 interface, see Figure 3c–e. We think this is mainly originated by the very efficient action of the substrate thermal treatment in reducing the Sb_2Te_3 surface roughness when grown on Si(111), as previously reported.[5] This condition leads to an almost epitaxial growth of Sb_2Te_3 with clear van der Waals layers already in the PRE ANN case.[5] As a consequence, the subsequent Fe growth occurs more regularly, with marginal chemical mixing, finally giving an almost pure magnetically-ordered Fe layer, comparable to a reference growth directly on Si(111), see Figure 3a,c,d. Therefore, the better structural quality of Sb_2Te_3 in the PRE ANN and POST ANN samples, when compared to AS-DEP (and to granular Sb_2Te_3 on SiO_2), has a major role in limiting the Fe chemical interaction with Te close to the Sb_2Te_3 surface. Additionally, a role could be also played by the higher energy of the impinging Fe atoms in the case of a pulsed laser deposition,[10] when compared to e-beam evaporation (present results). To develop a theoretical model for the evolution of the Fe/Sb_2Te_3 interface upon Sb_2Te_3 annealing is of certain interest, with a special focus on the thermally induced tuning of the chemical, structural or magnetic properties. We hope our results will further boost the use of first-principles multiscale modeling in this direction.[21]

2.3. Broadband FMR and Spin Pumping

FMR in Au/Fe/(Au/)Sb_2Te_3

BFMR is employed to study the magnetization dynamics of samples REF, AS DEP, PRE ANN, and POST ANN reported in Table 1, and the acquired data are depicted in **Figure 4**. For the AS DEP sample, the BFMR signal is too weak to be easily revealed, likely due to the disordered morphology of the Au/Fe bilayer, as emerged from the discussion of the XRR and CEMS data (Section 2.2). Figure 4a reports the evolution of the resonant frequency (f_{res}) as a function of the resonant magnetic field (H_{res}), which is interpreted with Equation (1), for all samples.

$$f_{res} = \frac{\gamma}{2\pi}\sqrt{H_{res}\left(H_{res}+4\pi M_{eff}\right)} \quad (1)$$

where γ is the gyromagnetic ratio and M_{eff} the effective magnetization. The M_{eff} value can be expressed as $4\pi M_{eff} = 4\pi M_s - H_{k,}$ where M_s and H_k are the saturation magnetization and the magnetic anisotropy field, respectively. The extracted M_{eff} (*g*-factor) values are 586±38 emu cc^{-1} (2.47±0,02) and 594±33 emu cc^{-1} (2.47±0,02) for the PRE ANN and POST ANN, respectively, and 682±42 emu cc^{-1} (2.56±0,02) for the REF sample, being lower than in bulk Fe (M_{eff} ≈1700 emu cc^{-1}). On the other hand, the XRR and CEMS results point to a relatively good quality of the Fe layers, therefore excluding a significant contribution from magneto-structural disorder and/or magnetic dead layers in reducing M_{eff}. We attribute the H_k increase mainly to surface-induced anisotropy.[22–24] Even in very sharp interfaces, an additional source of magnetic anisotropy can also originate from the hybridization occurring at the Au/Fe and Fe/Sb_2Te_3 interfaces, giving rise to a local modification of the materials band structure.[22]

Figure 4b summarizes the full width at half maximum (FWHM) ΔH of the BFMR signal as a function of f_{res}, and the linear fit is performed using Equation (2).

$$\Delta H = \Delta H_0 + \frac{4\pi\alpha}{\gamma} f_{res} \quad (2)$$

where α indicates the damping constant (or Gilbert parameter) and ΔH_0 the so-called inhomogeneous broadening term, a quantity accounting for the magneto-structural disorder present in a FM thin film.

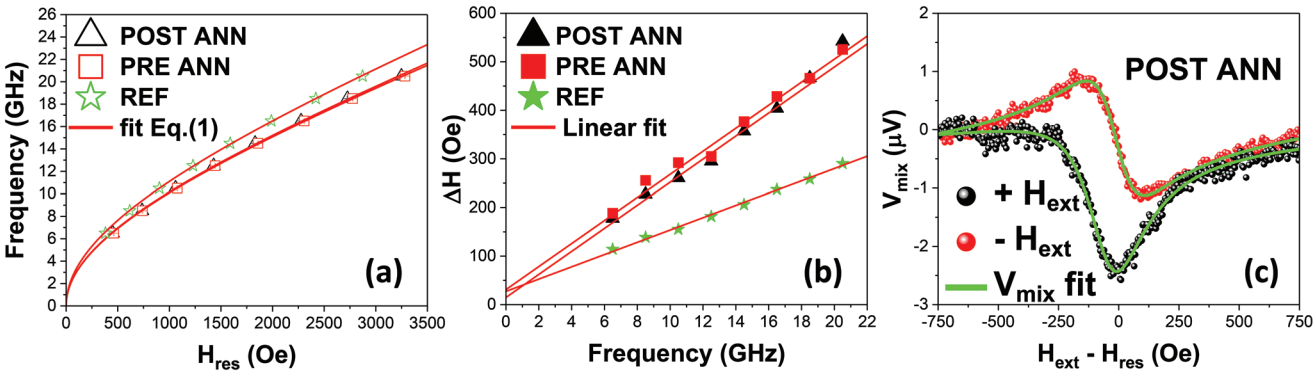

Figure 4. BFMR measurements on the REF, PRE ANN and POST ANN samples reported in Table 1. a) represents the evolution of the Kittel's curves in the in-plane (IP) configuration, from which γ and M_{eff} are extracted. In panel b), the BFMR signal linewidth as a function of the resonant frequency is plotted. The red solid lines indicate the linear fit from which α and ΔH_0 are extracted. c) V_{mix} acquired for the POST ANN sample at RF frequency of 12.5 GHz and RF power of 132 mW. The presence of an almost totally anti-symmetric signal for negative magnetic fields (red dots) indicates a negligible SP effect, as discussed in the main text.

For the PRE ANN and POST ANN samples $\alpha = 41 \cdot 10^{-3}$, representing a 44% enhancement when compared to the REF ($\alpha = 23 \cdot 10^{-3}$). Both the Kittel dispersion (Figure 4a), and the α values extracted for samples PRE ANN and POST ANN (Figure 4b), show that these two samples are magnetically very similar, which is in accordance with their almost identical chemical, structural and magnetic properties, as probed by XRR and CEMS (Section 2.2). The measured $\Delta H_0 < 30$ Oe for all samples (y-intercept in Figure 4b) is significantly lower or comparable with many reports present in the literature.[25–28] Again, this corroborates the good magneto-structural quality of the Fe layer anticipated by XRR and CEMS results.

Often, the increase of the FMR damping parameter α in FM/TI systems, when compared to FM-reference structures, is attributed to the generation of a pure spin current in the FM layer that is pumped orthogonally in the TI.[29–34] When this happens, following SP, a longitudinal charge current should be generated at the FM/TI interface. In the case of an occurring pure SP mechanism, the slope of the linear fit in Figure 4b is related to the so-called spin mixing conductance g_{eff}, as described by Equation (3).

$$g^{\uparrow\downarrow}_{eff,Sb_2Te_3} = \frac{4\pi M_s t_{FM}}{g\mu_B}\left(\alpha_{FM/TI} - \alpha_{FM}\right) \quad (3)$$

where μ_0 is the Bohr magneton, t_{FM} the thickness of the ferromagnetic layer, $\alpha_{FM/TI}$ and α_{FM} are the damping constant of the samples with and without the TI layer, respectively. g_{eff} is a fundamental figure of merit, which quantifies the spin current that accumulates at the FM/TI interface. Other than SP effects, an increased α value at FM/TI, when compared to FM, can also originate from a spin memory loss at the FM/TI interface and/or structural inhomogeneities of the FM layer.[35] The subtraction of a proper reference is considered a reliable strategy to exclude contributions not directly related to the SP process.[28,36] Indeed, this approach allows to eliminate the SP arising at the Au/Fe interface, thus isolating the contribution solely from the bottom Fe/Sb_2Te_3 interface. The two-magnon scattering (TMS) cannot be fully accounted for with the subtraction method, and it can generate an over- or under-estimation of g_{eff}.[4,35] On the other hand, our extracted g_{eff} value for both PRE ANN and POST ANN samples is $g_{eff} = 2.2 \cdot 10^{19}\ m^2$, being very well in accordance with those reported for similar heterostructures,[25–39] thus suggesting a negligible contribution of TMS at the Fe/Sb_2Te_3 interfaces.

In order to investigate the relationship between the measured g_{eff} in the POST ANN sample and the occurrence of S2C, and to estimate the SP efficiency, we refer to the procedure described in ref. [4]. In particular, SP-FMR is conducted on the POST ANN sample, and the results are depicted in Figure 4c. Here, the so-called mixing voltage (V_{mix}) is recorded, and the $V_{mix}(H_{res})$ curve is fitted with the Lorentzian function, Equation (4).

$$V_{mix} = V_{Sym}\frac{\Delta H^2}{\Delta H^2 + (H - H_{res})^2} + V_{Asym}\frac{\Delta H(H - H_{res})}{\Delta H^2 + (H - H_{res})^2} \quad (4)$$

where V_{sym} and V_{asym} are the symmetric and anti-symmetric components, respectively due to SP and rectification effects.[4] The symmetric contribution can also arise from the thermal Seebeck effect. Being such a thermal contribution independent from the H_{res} direction,[40] it can be eliminated by considering the effective SP signal (V_{SP}), as extracted by the following Equation (5).

$$V_{SP} = \frac{\left|V^{+H}_{Sym} - V^{-H}_{Sym}\right|}{2} \quad (5)$$

where V^{+H}_{Sym} and V^{-H}_{Sym} are the symmetric component of the V_{mix} curves acquired for positive and negative magnetic fields. Being dependent on the spin accumulation, the sign of the pure V_{SP} signal should reverse with the inversion of the magnetic field direction, but, as clearly shown in Figure 4c, this is not observed. The V_{mix} signal acquired for positive magnetic fields (black dots) certainly contains a symmetric contribution that is quantified with $V^{+H}_{Sym} = -2.08 \pm 0.03 \cdot 10^{-6}\ \mu V$. On the other hand, at negative magnetic fields (red dots), the symmetric contribution almost vanishes with a measured $V^{-H}_{Sym} = -5 \pm 2 \cdot 10^{-8}\ \mu V$.

Due to the absence of the V_{Sym} sign inversion by reversing the applied magnetic field (Figure 4c), we deduce about the

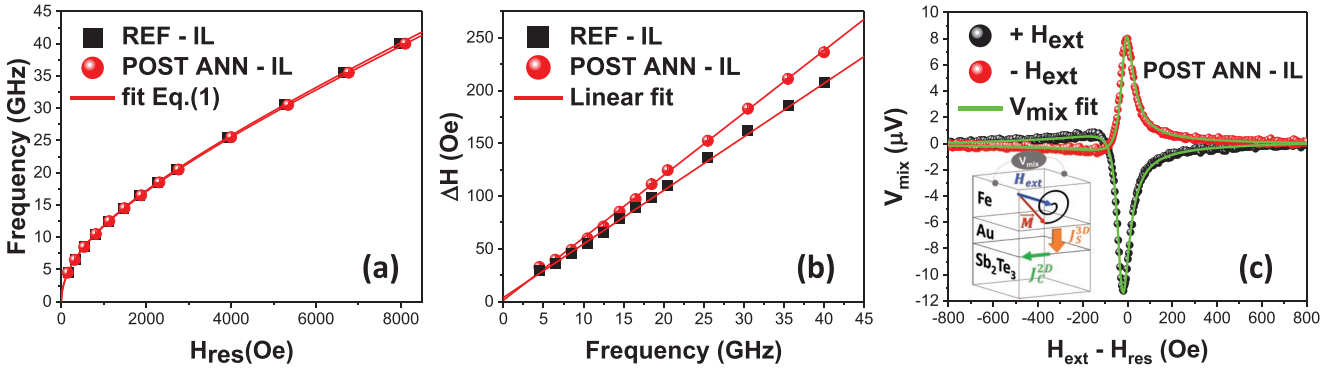

Figure 5. a) Kittel's curves for samples REF-IL and POST ANN-IL for the IP configuration. b) BFMR signal linewidth as a function of the resonant frequency for the same sample in panel (a). In c) the mixing voltage (V_{mix}) signal acquired for sample POST ANN-IL at RF-frequency of 12.5 GHz and RF-power of 90 mW is reported. The black and red dots indicate the V_{mix} acquired for positive and negative magnetic fields, respectively. The green solid line represents the best fits of the curves with Equation (4). The values extracted from the fit are discussed in the main text. The inset shows a scheme of the SP-FMR principle. Here, the precessing magnetization damps toward the direction of a quasi-static external magnetic field under the effect of a RF current generating a pure spin current (J_S^{3D}), subsequently converted in a longitudinal 2D charge current in the non-magnetic layer (NM) and revealed as a potential drop (V_{mix}) across the junction.

absence of any S2C in POST ANN. This happens despite the good structural and magnetic quality of such sample (Section 2.2), and the presence of a clear enhancement of the Gilbert damping constant α, as detected by BFMR when compared to the REF sample (Figure 4b). Our results constitute a clear warning in concluding about the occurrence of SP (i.e., a successful S2C) only on the basis of (B)FMR.[29–34] The enhanced α value is due to the large transverse 3D spin current density (J_S^{3D}) that is generated in the Fe layer when in contact with Sb_2Te_3. On the other hand, this is not converted into charge current through S2C conversion, suggesting that the high SOC in Sb_2Te_3 may not be sufficient to generate S2C.

It is well known how the nature of TSS is ideally preserved when TI are interfaced with non-magnetic materials (i.e., non-magnetic impurities), while the direct contact with FM layers could prevent the conservation of the TSS.[36,41,42] In the case of S2C mainly occurring through the TSS, it would then be clear how such a process can be detrimentally affected when interfacing Fe with Sb_2Te_3. To get more insight into the above scenario, we conduct BFMR and SP-FMR on POST ANN-IL and REF-IL, where an Au interlayer between Fe and Sb_2Te_3 is used to protect the TSS (Table 1), and the results are summarized in **Figure 5**.

From the analysis of the Kittel dispersion (Figure 5a), the extracted M_{eff} (*g*-factor) values are 1183±15 emu cc^{-1} (2.12±0,01) and 1213±11 emu cc^{-1} (2.01±0,01) for the POST ANN-IL and REF-IL, respectively. When compared to the set of samples without the Au interlayer (Table 1), the M_{eff} values are almost doubled. Due to the similar chemical, structural, and magnetic quality of the Fe layers in POST ANN and POST ANN-IL (Section 2.2), we attribute such a higher M_{eff} to a strong reduction of the surface magnetic anisotropy due to the Au interlayer. Also the lower *g*-factors, when compared to the samples without Au interlayer, are in accordance with the higher crystallographic symmetry of the Fe/Au interface with respect to Fe/Sb_2Te_3, being characterized by a body center cubic (BCC)/BCC and BCC/rhombohedral symmetry, respectively.[22]

Figure 5b shows the corresponding $\Delta H(f_{res})$ curves for the POST ANN-IL and REF-IL samples. From the linear fit with Equation (2), it emerges that both samples have an extremely low $\Delta H_0 < 4$ Oe, an indication of a very good magneto-structural quality. POST ANN-IL shows $\alpha = 8.75 \cdot 10^{-3}$, higher than the $\alpha = 7.35 \cdot 10^{-3}$ in REF-IL. Such a measured $\Delta\alpha = 1.4 \cdot 10^{-3}$ generates a spin mixing conductance $g_{eff} = 5.3 \cdot 10^{18}$ m^{-2}, a value which is 76% lower than in POST ANN. Such a reduction is due to the introduction of the Au interlayers, which give rise to additional dissipative phenomena for the produced spin current (i.e., interfacial spin memory loss, scattering with impurities, thermal dissipation).[43] The almost perfect superposition of the Kittel curves showed in Figure 5a and the $\Delta H_0 < 4$ Oe value extracted from Figure 5b further confirm that the Au/Fe/Au trilayers deposited on Sb_2Te_3 and Si(111) substrates, have almost the same magneto-structural properties, a fundamental prerequisite to make a reliable comparison between the two cases, to estimate the S2C due to the presence of Sb_2Te_3.

To directly evaluate the S2C efficiency in the POST ANN-IL sample, SP-FMR experiments are conducted. According to Equation (6) (see Experimental Section), the produced spin current density is $J_S^{3D} = 1.15 \cdot 10^6\ Am^{-2}$. In Figure 5c the V_{mix} signal acquired for sample POS ANN-IL is reported, together with a schematic representation of the SP-FMR experiment in the inset. From the fit of the data reported in Figure 5c, $V_{SP} = 9.32$ μV is obtained, from which we calculate a generated 2D charge current $J_C^{2D} = V_{SP}/RW = 0.31$ mA m^{-1}, where $R = 16.8$ Ohm is the resistivity value measured in four-point configuration and $W = 1.8 \cdot 10^{-3}$ m is the width of the sample. By comparing Figure 5c with Figure 4c for the POST ANN, it is clear that a large V_{SP} appears thanks to the Au insertion, which clearly changes sign upon the reversal of the applied magnetic field, thus demonstrating the occurrence of S2C.

Our results demonstrate that the observed S2C cannot originate from a bulk spin Hall effect in Sb_2Te_3, otherwise it should be observed in POST ANN as well. The immediate explanation is that inserting a 5 nm Au layer between Fe and Sb_2Te_3 protects the TSS in Sb_2Te_3 (Figure 1), finally allowing to electrically detect S2C. This is in accordance with what we have previously observed in Co/Sb_2Te_3 systems,[4] thus showing that the S2C is

not dependent on the FM nature (Fe or Co). Indeed, the successful use of Au in protecting the TSS of other TI (Bi_2Se_3) has been previously suggested,[44] with basically unaltered spin-momentum locking shown in Au/Bi_2Se_3. When compared to other metals such as Ag or Cr, Au has turned out to be more efficient in producing a chemically-inert Au/Bi_2Se_3 interface.[44–46] Our results show that this may well be the case also in the Au/Sb_2Te_3 system.

Within the above scenario, the S2C can be described by the so-called Inverse Edelstein Effect (IEE),[47,48] where the IEE length $\lambda_{IEE} = \frac{J_C^{2D}}{J_S^{3D}}$ represents the figure of merit to quantify the S2C efficiency. For sample POST ANN-IL we obtain λ_{IEE} = 0.27 nm, which is in perfect agreement with the value obtained in Au/Co/Au/Sb_2Te_3,[4] thus demonstrating the intrinsic role played by Sb_2Te_3 and its preserved TSS to origin such a large S2C. When compared to other 2nd class chalcogenide-based TI,[26,37–39,48–54] the extracted λ_{IEE} is comparable to the highest reported so far.

Our results show that realizing a chemically and magnetically pure Fe/Sb_2Te_3 interface may not be enough to achieve a successful S2C, which is, on the other hand, achieved through the insertion of an Au interlayer to protect the TSS of Sb_2Te_3.

3. Conclusion

In summary, MC experiments show that the annealed epitaxial Sb_2Te_3 develops TSS-connected conduction. When interfaced with Fe, the enhanced chemical-structural quality of Sb_2Te_3 is connected to a remarkable suppression of intermixing occurring at the Fe/Sb_2Te_3 interface. Indeed, BFMR evidences that such an enhanced chemical, structural and magnetic quality of the Fe/Sb_2Te_3 interface gives rise to a clear broadening of the magnetic damping, which is often attributed to a successful S2C. However, our results show that this may not be the case, since no S2C is electrically detected in Fe/Sb_2Te_3 samples. On the other hand, the use of an Au interlayer at the Fe/Sb_2Te_3 interface turns out to be successful in achieving quite a large S2C, thus strongly suggesting that the observed effect mainly relates to the TSS of Sb_2Te_3, which are finally driving S2C, due to the IEE. We extract quite a large λ_{IEE} = 0.27 nm conversion factor, in very good agreement with what we have observed by using an Au/Co/Au injector on top of Sb_2Te_3.[4] This demonstrates that a successful S2C conversion can be achieved in Sb_2Te_3-based systems by employing an Au interlayer, and such a conversion does not depend on the nature of the FM electrode (Fe, Co).

4. Experimental Section

Sb_2Te_3 thin films were grown by MOCVD with an AIXTRON 200/4 setup operating with ultra-pure nitrogen carrier gas and equipped with a cold wall horizontal deposition chamber, accommodating a 4'' IR-heated graphite susceptor. The Sb_2Te_3 crystalline quality improved by appropriate thermal treatment of the substrate (at 500 °C) prior to the deposition (PRE ANN sample in Table 1), followed by in situ post-deposition annealing at 300 °C (POST ANN sample in Table 1). All the details about the Sb_2Te_3 samples preparation can be found in ref. [5].

Prior to the deposition of Fe, resistivity and MC measurements were carried out on the Sb_2Te_3 thin films by using a four points probe with the van der Pauw method, by making use of a closed-cycle cryostat.[11] Magnetic fields up to 0.8 T were applied and directed perpendicularly with respect to the sample plane (and the current). The MC measurements were conducted at a constant applied current (50 μA into the as-deposited and 100 μA in the pre- and post-annealed Sb_2Te_3), by measuring the voltage changes during the magnetic field scan. In particular, the measurements of the sheet resistance (R_S) as a function of the magnetic field (B) and temperature (T) were recorded on $1 \times 1\,cm^2$ substrates cleaved from the grown wafers without any patterning, thus avoiding potential additional surface degradations.

Following MC, the Sb_2Te_3/Si(111) pieces were transferred into an Edwards Auto306 e-beam evaporation tool, where the Au(5 nm)/^{57}Fe (5 nm) bilayers and Au(5 nm)/^{57}Fe(5 nm)/Au(5 nm) trilayers were deposited all in situ. In all the processes the starting value of the vacuum in the deposition chamber was in the range of $5 \cdot 10^{-7} \div 10^{-6}$ Pa. For each evaporated element, the electronic gun deposition currents and the corresponding chamber pressures during the growths were for Au: 120 mA and $7.8 \cdot 10^{-6}$ Pa; for Fe: 80 mA and $4.6 \cdot 10^{-6}$ Pa. The Si(111) substrates used as references were cleaned with isopropyl alcohol and treated with HF prior to the evaporation processes.

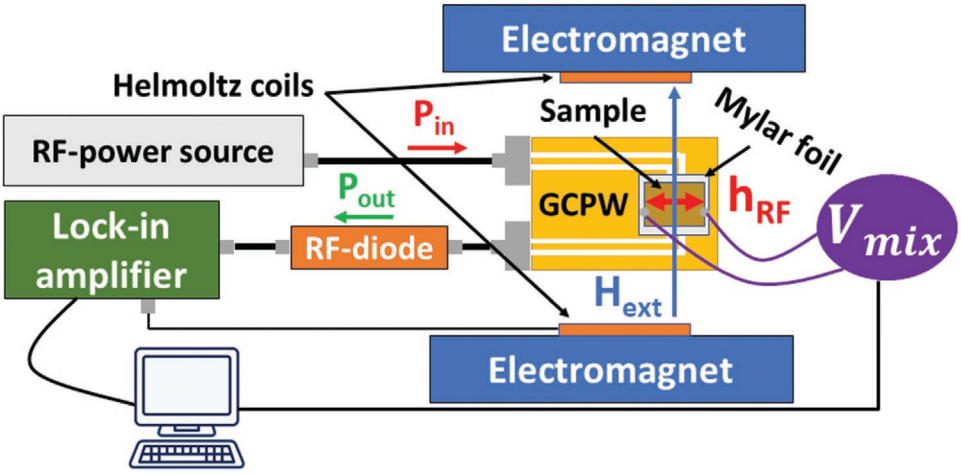

Figure 6. Scheme of the experimental setup used for BFMR and SP-FMR experiments. For more details on the technical aspect of these measurements please refer to ref. [4].

X-Ray Reflectivity (XRR) analysis was conducted by using a Cu radiation with the K_α emission at λ = 1.54 Å and the patterns were collected with a commercial scintillator and modelled through a matrix formalism corrected by a Croce-Nevot factor. XRR measurements allowed the determination of the thickness, the roughness, and the electronic density (ρ_e) of each layer composing the sample. In particular, ρ_e is related to the measured critical vector Qc by the relation Qc (Å^{-1}) = $0.0375\sqrt{\rho_e(e^-/\text{Å}^3)}$ (for the Cu K_α emission).[55]

The isotopically enriched ^{57}Fe layer allowed to perform CEMS analysis,[10] which was carried out at RT on all samples in Table 1. CEMS was conducted in a constant-acceleration drive, with the sample mounted as an electrode in a parallel-plate avalanche detector filled with acetone gas. An α-Fe foil at RT was used for the CEMS velocity scale calibration and all the reported isomer shifts are relative to α-Fe. The relative area fraction in Figure 3e was obtained by assuming the same Debye-Waller factor f = 1 for all the components. Analysis of the CEMS data was carried out with the Vinda software package.[56]

BFMR was conducted by a broadband Anritsu-MG3694C power source (1–40 GHz), connected to a home-made grounded coplanar waveguide (GCPW), where the samples were mounted in a flip-chip configuration (with the FM film close to the GCPW surface) with a 20 µm thick mylar foil stacked in between to avoid the shortening of the conduction line. The sample-GCPW system was positioned between the polar extensions of a Bruker ER-200 electromagnet maintaining its surface parallel to the external magnetic field H_{ext}, in the so called in-plane (IP) configuration. During the measurements, an RF current at a fixed frequency was carried toward the GCPW and the transmitted signal was directed to a rectifying diode (Wiltron, Model 70KB50 NEG) which converts the RF-signal in a continuous DC-current, subsequently detected by a lock-in amplifier downward the electronic line. A scheme of the BFMR facility is shown in **Figure 6**. The same instrumental setup adopted for BFMR was employed to perform SP-FMR measurements. In this case, the edges of the sample were contacted with Ag paint and connected to a nanovoltmeter. For a fixed RF frequency and power, a DC-voltage was detected when the FMR occurred (see Figure 6).

For the SP-FMR measurements carried out in this manuscript, the RF frequency was fixed at 12.5 GHz and the RF power varied from 90 to 132 mW. According to the different RF power, the generated 3D spin current J_S^{3D} (in units of A m^{-2}) was calculated by using Equation (6).

$$J_S^{3D} = \frac{Re\left(g_{\text{eff}}^{\uparrow\downarrow}\right)\gamma^2 h_{RF}^2 \hbar}{8\pi\alpha^2}\left(\frac{\mu_0 M_S - \sqrt{(\mu_0 M_S)^2 + 4\omega^2}}{(4\pi M_S\,\gamma)^2 + 4\omega^2}\right)\frac{2e}{\hbar} \quad (6)$$

where $\hbar$ is the reduced Plank constant, M_S the saturation magnetization, ω the frequency of the RF-signal, e the charge of the electron and h_{RF} the transverse oscillating magnetic field generated by the GCPW.

Supporting Information

Supporting Information is available from the Wiley Online Library or from the author.

Acknowledgements

The authors acknowledge the Horizon 2020 project SKYTOP "Skyrmion-Topological Insulator and Weyl Semimetal Technology" (FETPROACT-2018-01, n. 824123). The authors thank Dr. Lucia Nasi for providing the original AFM data previously reported,[11] Dr. Martino Rimoldi, Dr. Raimondo Cecchini and Dr. Claudia Wiemer for their contribution to the development of epitaxial Sb_2Te_3,[5,6] and Prof. Tobias Kampfrath for fruitful discussions.

Open Access Funding provided by Consiglio Nazionale delle Ricerche within the CRUI-CARE Agreement.

Conflict of Interest

The authors declare no conflict of interest.

Data Availability Statement

Research data are not shared.

Keywords

conversion electron Mössbauer spectroscopy, ferromagnetic resonance, magnetotransport, spin-charge conversion, spin pumping, topological insulators

Received: July 15, 2021
Revised: September 3, 2021
Published online: November 5, 2021

[1] A. Soumyanarayanan, N. Reyren, A. Fert, C. Panagopoulos, *Nature* **2016**, *539*, 509.
[2] F. Hellman, A. Hoffmann, Y. Tserkovnyak, G. S. D. Beach, E. E. Fullerton, C. Leighton, A. H. Macdonald, D. C. Ralph, D. A. Arena, H. A. Dürr, P. Fischer, J. Grollier, J. P. Heremans, T. Jungwirth, A. V. Kimel, B. Koopmans, I. N. Krivorotov, S. J. May, A. K. Petford-Long, J. M. Rondinelli, N. Samarth, I. K. Schuller, A. N. Slavin, M. D. Stiles, O. Tchernyshyov, A. Thiaville, B. L. Zink, *Rev. Mod. Phys.* **2017**, *89*, 25006.
[3] J. Sinova, S. O. Valenzuela, J. Wunderlich, C. H. Back, T. Jungwirth, *Rev. Mod. Phys.* **2015**, *87*, 1213.
[4] E. Longo, M. Belli, M. Alia, M. Rimoldi, R. Cecchini, M. Longo, C. Wiemer, L. Locatelli, P. Tsipas, A. Dimoulas, G. Gubbiotti, M. Fanciulli, R. Mantovan, *Adv. Funct. Mater.* **2021**, 2109361, https://10.1002/adfm.202109361.
[5] M. Rimoldi, R. Cecchini, C. Wiemer, A. Lamperti, E. Longo, L. Nasi, L. Lazzarini, R. Mantovan, M. Longo, *RSC Adv.* **2020**, *10*, 19936.
[6] A. Kumar, R. Cecchini, L. Locatelli, C. Wiemer, C. Martella, L. Nasi, L. Lazzarini, R. Mantovan, M. Longo, *Cryst. Growth Des.* **2021**, 7, 4023.
[7] E. Longo, C. Wiemer, R. Cecchini, M. Longo, A. Lamperti, M. Fanciulli, R. Mantovan, E. Longo, M. Fanciulli, A. Khanas, A. Zenkevich, *J. Magn. Magn. Mater.* **2019**, *474*, 632.
[8] T. L. Anderson, H. B. Krause, *Acta Crystallogr., Sect. B: Struct. Crystallogr. Cryst. Chem.* **1974**, *30*, 1307.
[9] H. Zhang, C. X. Liu, X. L. Qi, X. Dai, Z. Fang, S. C. Zhang, *Nat. Phys.* **2009**, *5*, 438.
[10] E. Longo, C. Wiemer, R. Cecchini, M. Longo, A. Lamperti, A. Khanas, A. Zenkevich, M. Cantoni, C. Rinaldi, M. Fanciulli, R. Mantovan, *Adv. Mater. Interfaces* **2020**, *7*, 2000905.
[11] R. Cecchini, R. Mantovan, C. Wiemer, L. Nasi, L. Lazzarini, M. Longo, *Phys. Status Solidi RRL* **2018**, *12*, 1800155.
[12] H.-Z. Lu, S.-Q. Shen, in *Spintronics VII* (Eds: H.-J. Drouhin, J.-E. Wegrowe, M. Razeghi), SPIE, Bellingham, WA **2014**, p. 91672E.
[13] S. P. Chiu, J. J. Lin, *Phys. Rev. B.* **2013**, *87*, 035122.
[14] A. Roy, S. Guchhait, S. Sonde, R. Dey, T. Pramanik, A. Rai, H. C. P. Movva, L. Colombo, S. K. Banerjee, *Appl. Phys. Lett.* **2013**, *102*, 163118.
[15] K. Shrestha, M. Chou, D. Graf, H. D. Yang, B. Lorenz, C. W. Chu, *Phys. Rev. B* **2017**, *95*, 195113.
[16] J. Daillant, A. Gibaud, *X-ray and Neutron Reflectivity: Principles and Applications*, Springer, Berlin **1999**, p. 331.
[17] M. Przybylski, J. Korecki, U. Gradmann, *Hyperfine Interact.* **1990**, *57*, 2053.

[18] A. Błachowski, K. Ruebenbauer, J. Przewoźnik, J. Zukrowski, *J. Alloys Compd.* **2008**, *458*, 96.
[19] A. Zenkevitch, M. Fanciulli, G. Weyer, I. Khabelashvili, *Phys. Status Solidi B* **2000**, *222*, 279.
[20] M. Fanciulli, C. Rosenblad, G. Weyer, H. Von Kanel, N. Onda, V. Nevolin, A. Zenkevich, in *Materials Research Society Symp. – Proc.*, Materials Research Society, Warrendale, PA **1996**, pp. 319–324.
[21] B. Mortazavi, E. V. Podryabinkin, S. Roche, T. Rabczuk, X. Zhuang, A. V. Shapeev, *Mater. Horiz.* **2020**, *7*, 2359.
[22] M. Farle, *Rep. Prog. Phys.* **1998**, *61*, 755.
[23] E. Longo, C. Wiemer, M. Belli, R. Cecchini, M. Longo, M. Cantoni, C. Rinaldi, M. D. Overbeek, C. H. Winter, G. Gubbiotti, G. Tallarida, M. Fanciulli, R. Mantovan, *J. Magn. Magn. Mater.* **2020**, *509*, 166885.
[24] C. Chappert, K. L. Dang, P. Beauvillain, H. Hurdequint, D. Renard, *Phys. Rev. B* **1986**, *34*, 3192.
[25] F. Bonell, M. Goto, G. Sauthier, J. F. Sierra, A. I. Figueroa, M. V. Costache, S. Miwa, Y. Suzuki, S. O. Valenzuela, *Nano Lett.* **2020**, *20*, 5893.
[26] M. Jamali, J. S. Lee, J. S. Jeong, F. Mahfouzi, Y. Lv, Z. Zhao, B. K. Nikolić, K. A. Mkhoyan, N. Samarth, J. P. Wang, *Nano Lett.* **2015**, *15*, 7126.
[27] B. L. Zink, M. Manno, L. O'Brien, J. Lotze, M. Weiler, D. Bassett, S. J. Mason, S. T. B. Goennenwein, M. Johnson, C. Leighton, *Phys. Rev. B* **2016**, *93*, 184401.
[28] A. Ruiz-Calaforra, T. Brächer, V. Lauer, P. Pirro, B. Heinz, M. Geilen, A. V. Chumak, A. Conca, B. Leven, B. Hillebrands, *J. Appl. Phys.* **2015**, *117*, 163901.
[29] M. Morota, Y. Saito, N. Uchida, *Phys. Status Solidi RRL* **2021**, *15*, 2100247.
[30] M. Tokaç, S. A. Bunyaev, G. N. Kakazei, D. S. Schmool, D. Atkinson, A. T. Hindmarch, *Phys. Rev. Lett.* **2015**, *115*, 056601.
[31] C. T. Boone, H. T. Nembach, J. M. Shaw, T. J. Silva, *J. Appl. Phys.* **2013**, *113*, 153906.
[32] A. A. Baker, A. I. Figueroa, L. J. Collins-Mcintyre, G. Van Der Laan, T. Hesjedal, *Sci. Rep.* **2015**, *5*, 7907.
[33] A. Ghosh, J. F. Sierra, S. Auffret, U. Ebels, W. E. Bailey, *Appl. Phys. Lett.* **2011**, *98*, 052508.
[34] T. G. A. Verhagen, H. N. Tinkey, H. C. Overweg, M. Van Son, M. Huber, J. M. Van Ruitenbeek, J. Aarts, *J. Phys.: Condens. Matter* **2016**, *28*, 056004.
[35] L. Zhu, D. C. Ralph, R. A. Buhrman, *Phys. Rev. Lett.* **2019**, *123*, 57203.
[36] J. C. R. Sánchez, L. Vila, G. Desfonds, S. Gambarelli, J. P. Attané, J. M. De Teresa, C. Magén, A. Fert, *Nat. Commun.* **2013**, *4*, 2944.
[37] M. Dc, J. Y. Chen, T. Peterson, P. Sahu, B. Ma, N. Mousavi, R. Harjani, J. P. Wang, *Nano Lett.* **2019**, *19*, 4836.
[38] P. Deorani, J. Son, K. Banerjee, N. Koirala, M. Brahlek, S. Oh, H. Yang, *Phys. Rev. B* **2014**, *90*, 094403.
[39] J. B. S. Mendes, O. Alves Santos, J. Holanda, R. P. Loreto, C. I. L. De Araujo, C. Z. Chang, J. S. Moodera, A. Azevedo, S. M. Rezende, *Phys. Rev. B* **2017**, *96*, 180415.
[40] K. I. Uchida, H. Adachi, T. Ota, H. Nakayama, S. Maekawa, E. Saitoh, *Appl. Phys. Lett.* **2010**, *97*, 172505.
[41] A. K. Kaveev, A. G. Banshchikov, A. N. Terpitskiy, V. A. Golyashov, O. E. Tereshchenko, K. A. Kokh, D. A. Estyunin, A. M. Shikin, *Semiconductors* **2020**, *54*, 1051.
[42] M. Z. Hasan, C. L. Kane, *Rev. Mod. Phys.* **2010**, *82*, 3045.
[43] K. Nakahashi, K. Takaishi, T. Suzuki, K. Kanemoto, *ACS Appl. Electron. Mater.* **2021**, *4*, 1663.
[44] C. D. Spataru, F. Léonard, *Phys. Rev. B: Condens. Matter Mater. Phys.* **2014**, *90*, 3.
[45] K. Ferfolja, M. Valant, I. Mikulska, S. Gardonio, M. Fanetti, *J. Phys. Chem. C* **2018**, *122*, 9980.
[46] M. Fanetti, I. Mikulska, K. Ferfolja, P. Moras, P. M. Sheverdyaeva, M. Panighel, A. Lodi-Rizzini, I. Píš, S. Nappini, M. Valant, S. Gardonio, *Appl. Surf. Sci.* **2019**, *471*, 753.
[47] V. M. Edelstein, *Solid State Commun.* **1990**, *73*, 233.
[48] J. C. Rojas-Sánchez, S. Oyarzún, Y. Fu, A. Marty, C. Vergnaud, S. Gambarelli, L. Vila, M. Jamet, Y. Ohtsubo, A. Taleb-Ibrahimi, P. Le Fèvre, F. Bertran, N. Reyren, J. M. George, A. Fert, *Phys. Rev. Lett.* **2016**, *116*, 096602.
[49] M. Dc, T. Liu, J. Y. Chen, T. Peterson, P. Sahu, H. Li, Z. Zhao, M. Wu, J. P. Wang, *Appl. Phys. Lett.* **2019**, *114*, 102401.
[50] Y. Shiomi, K. T. Yamamoto, R. Nakanishi, T. Nakamura, S. Ichinokura, R. Akiyama, S. Hasegawa, E. Saitoh, *Appl. Phys. Lett.* **2018**, *113*, 052401.
[51] J. B. S. Mendes, M. Gamino, R. O. Cunha, J. E. Abrao, S. M. Rezende, A. Azevedo, *Phys. Rev. Mater.* **2021**, *5*, 024206.
[52] K. T. Yamamoto, Y. Shiomi, K. Segawa, Y. Ando, E. Saitoh, *Phys. Rev. B* **2016**, *94*, 024404.
[53] H. Wang, J. Kally, J. S. Lee, T. Liu, H. Chang, D. R. Hickey, K. A. Mkhoyan, M. Wu, A. Richardella, N. Samarth, *Phys. Rev. Lett.* **2016**, *117*, 076601.
[54] R. Sun, S. Yang, X. Yang, A. Kumar, E. Vetter, W. Xue, Y. Li, N. Li, Y. Li, S. Zhang, B. Ge, X. qun Zhang, W. He, A. F. Kemper, D. Sun, Z. hua Cheng, *Adv. Mater.* **2020**, *32*, 2005315.
[55] C. Wiemer, S. Ferrari, M. Fanciulli, G. Pavia, L. Lutterotti, *Thin Solid Films* **2004**, 450, 134.
[56] H. P. Gunnlaugsson, *Hyperfine Interact.* **2016**, *237*, 13.